ENGINEERING Agriculture

Engineering Journals

RESEARCH ARTICLE

2027 / Volume 14 / Issue 3 / 27736

Development and optimization of an orchard green-manure chopping and incorporation machine using rigid-flexible coupling simulation and field validation

Chun WANG[2], Yujing ZHOU[1], Yizhe YANG[1], Yongchao SHAO[1], Weiguo ZHANG (✉)[1]

1 College of Mechanical and Electronic Engineering, Northwest A&F University, Yangling 712100, China.
2 College of Biological and Agricultural Engineering, Jilin University, Changchun 130015, China.

KEYWORDS

Orchard green manure, rigid–flexible coupling, multibody dynamics, field experiment, parameter optimization

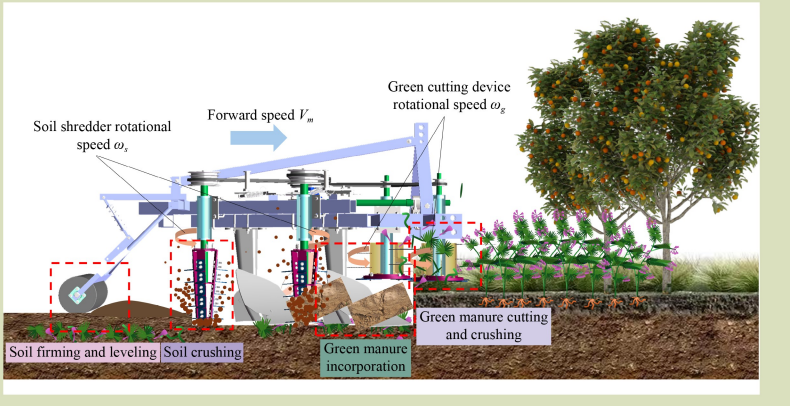
HIGHLIGHTS

- A manure chopping machine designed for hairy vetch management in dwarf apple orchards.
- Single-pass machine integrates cutting, incorporation, soil crushing and leveling.
- ADAMS/OptiStruct coupling modeled blade-stem interaction and fracture.
- Structural safety was verified under four extreme operating conditions.
- Field optimization achieved 91% cutting rate and 91% incorporation rate.

Received March 27, 2026;
Accepted July 8, 2026.

Correspondence: Zhangwg2026@163.com

GRAPHICAL ABSTRACT



ABSTRACT

To address inadequate stem chopping, shallow incorporation and multi-pass operation in existing orchard green-manure equipment, a dedicated machine for hairy vetch in dwarf apple orchards was developed to perform stem chopping and incorporation, soil pulverization and firming in a single pass. The overall structure and key components, including the green-manure chopping device, incorporation plow and soil-pulverizing device, were designed through theoretical analysis. ADAMS multibody dynamics models and an ADAMS/OptiStruct rigid-flexible contact model were used to analyze stem fracture during chopping, and finite-element analysis was used to verify structural strength under extreme conditions. Box-Behnken field experiments were then conducted to optimize operating parameters using the qualified stem-length rate and stem incorporation rate as response variables. Simulation results showed that the main load-bearing members of the machine were made of Q345 steel (yield strength 345 MPa) and satisfied the strength requirements under extreme conditions, with a maximum stress of 251 MPa

and a minimum safety factor of 1.37. The optimum practical settings were a forward speed of 1.1 m·s^{-1}, gearbox output shaft rotational speed of 450 r·min^{-1}, and incorporation depth of 190 mm; under these settings, the qualified stem-length rate was 91% ± 1.5% and the stem incorporation rate was 91% ± 2.1%.

© The Author(s) 2027. Published by Higher Education Press. This is an open access article under the CC BY license (http://creativecommons.org/licenses/by/4.0)

1 Introduction

Green manure refers to the green biomass of crops that is either wholly or partially incorporated into the soil during growth to improve soil fertility, increase organic-matter content, and enhance nutrient cycling[1,2]. Its beneficial effects arise mainly from biological nitrogen fixation, nutrient release and organic-matter accumulation[3–5]. Together, these processes improve soil structure and fertility, regulate soil pH, stimulate microbial activity and, to some extent, suppress pests and weeds[6,7]. China has long had the largest total orchard area globally. However, compared with the vast orchard area, the use of green-manure remains low. The national green-manure planting area is currently about 4.5 Mha, less than one-tenth of the potentially developable area in China. In terms of mechanization, the comprehensive mechanization rate of orchards in China is below 30%, which is markedly lower than the national crop tillage-sowing-harvesting comprehensive mechanization rate of 73% over the same period, and dedicated machinery for orchard green-manure chopping and incorporation is particularly scarce. This indicates that developing dedicated orchard green-manure chopping and incorporation equipment is of practical significance for increasing the use of green-manure and advancing orchard mechanization.

However, specialized orchard green-manure machinery suitable for hilly and mountainous regions remains limited, particularly machines capable of integrating stem chopping and incorporation, soil pulverization and firming in a single pass[8–10]. Zhang et al.[11] developed an inter-row chopping device for orchards to improve the chopping and incorporation performance of existing machines. Their machine can chop green manure, incorporate it into the soil and convey material within the furrow. However, it still provides insufficient incorporation depth, lacks a soil-firming unit and has poor soil-inversion performance at the furrow-opening blades, resulting in limited incorporation efficiency. Wang et al.[12] designed a combined rotary-tillage and seeding implement for green manure in trunk-type orchards in Xinjiang, using high-speed rotary blades to chop inter-row weeds and dead branches, thereby creating favorable conditions for subsequent sowing. Zhao et al.[13] proposed an inter-row green-manure chopping machine to address the difficulties in stem chopping, high operating costs and low field efficiency. Although the device can perform stem chopping and incorporation, and soil firming simultaneously, its incorporation rate remains low and it mainly targets aboveground biomass. Consequently, additional tillage equipment is still required to bury the chopped stems, resulting in a complicated multi-pass operation. A specialized orchard green-manure machine capable of integrated single-pass stem chopping and incorporation, soil pulverization and firming is therefore still needed.

To address the poor operational adaptability, inadequate stem chopping, and shallow incorporation depth of existing machines, this study focuses on hairy vetch intercropped in dwarf apple orchards in Shaanxi Province and develops a dedicated orchard green-manure machine that completes stem chopping and incorporation, soil pulverization and firming in a single pass. This study makes three main contributions. First, functional integration was achieved at the structural level, with stem chopping and incorporation, soil pulverization and firming performed together in one pass, overcoming the shallow incorporation depth and multi-pass operation of existing equipment. Second, to address the limitation that flexible bodies in ADAMS cannot directly simulate stem fracture, a fracture-controlled rigid-flexible coupling modeling method was proposed. This method combines flexible-body modeling with six-component force/torque connections, force/torque sensors and logic control functions, reproducing the deformation and fracture of hairy vetch stems. Third, a coupled ADAMS multibody dynamic and OptiStruct finite-element analysis framework was established, and the operating parameters were optimized and validated through a field Box-

Behnken test. The results provided a basis for the design and parameter selection of single-pass orchard green-manure chopping and incorporation equipment.

2 Materials and methods

2.1 Orchard green-manure planting patterns and agronomic requirements for incorporation

As shown in Fig. 1, dwarf apple orchards typically have row spacings of 3.5–4.5 m, trunk heights of 0.6–0.9 m and canopy diameters of 1.5–2.0 m. The effective inter-row width available for machinery is 1.5–2.5 m. At full flowering, hairy vetch usually reaches a natural height of 0.4–0.6 m. To prevent vigorous green-manure crops from climbing onto the trunks and competing for nutrients, the crop should be sown outside the canopy projection, about 1.0 m from the tree rows on both sides. Taking these agronomic requirements into account, the inter-row green-manure strip width was set at about 1.5 m[14–16].

2.2 Structure and working principle of the machine

As illustrated in Fig. 2, the orchard green-manure chopping and incorporation machine mainly consists of a frame, gearbox, parallel four-bar adjustment mechanism, belt-drive system, firming wheel, soil-pulverizing devices, incorporation plow, depth-limiting wheel and green-manure chopping devices. Power is transmitted from the tractor PTO (power take-off) shaft to the gearbox, where the rotational speed is reduced and torque is increased. The output is then delivered through the belt-drive system to the two front-mounted chopping devices and the two soil-pulverizing devices located behind the incorporation plow. The green-manure chopping devices, soil-pulverizing devices, and incorporation plow are mounted on the frame, and their positions and heights can be adjusted as required.

As illustrated in Fig. 3, the machine operates as follows. Before operation, the depth-limiting wheel is adjusted to achieve the required plowing and incorporation depth. The machine is attached to the tractor through a three-point hitch and moves forward at a constant speed. The front-mounted chopping devices chop the hairy vetch canopy and stems at the base, throwing the chopped stems to the right side. The incorporation plow then lifts and inverts the soil, burying the chopped stems beneath the surface. The soil-pulverizing devices subsequently pulverize the clods produced during plowing, and the rear firming wheel completes the firming process. In this way, the machine performs stem chopping and incorporation, soil pulverization and firming in a single pass.

2.3 Key component design and parameter determination

2.3.1 Design of green-manure chopping device

2.3.1.1 Structure and working principle of the green-manure chopping device

As illustrated in Fig. 4, the green-manure chopping device

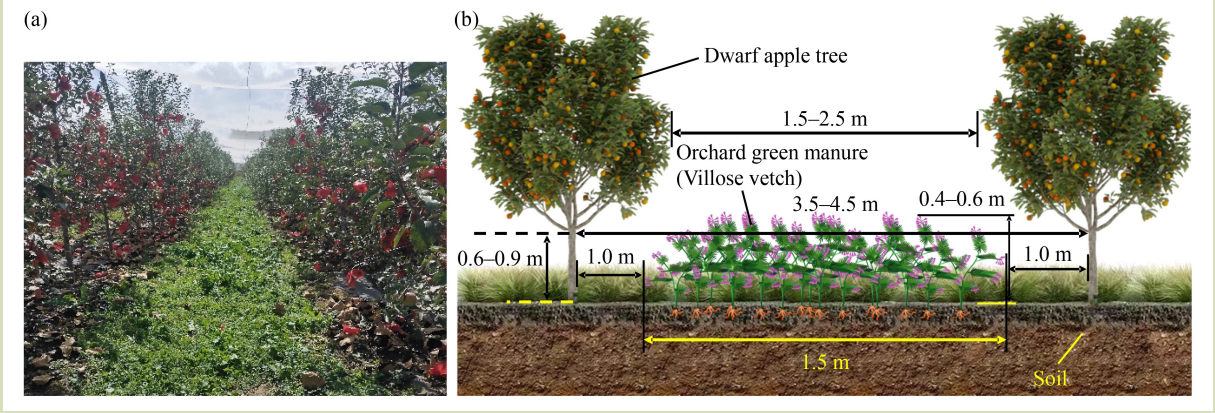


Fig. 1 (a) Dwarf apple orchards and (b) agronomic layout of hairy vetch green manure in dwarf apple orchards.

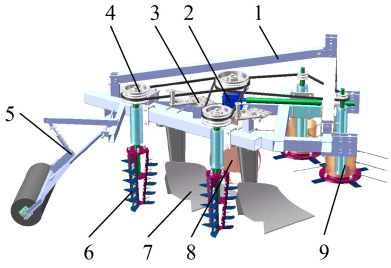


Fig. 2 Overall structural diagram of the orchard green-manure chopping and incorporation machine: 1, frame; 2, gearbox; 3, parallel four-bar adjustment mechanism; 4, belt-drive system; 5, firming wheel; 6, soil-pulverizing device; 7, incorporation plow; 8, depth-limiting wheel; and 9, chopping device.

mainly comprises a blade shaft, a V-belt pulley, chopping blades, a chopping disk, flexible chopping ropes, a fixed cylindrical housing and a cutter shaft sleeve. The chopping blades are bolted to the chopping disk, which is rigidly connected to the cylindrical housing. The blade shaft passes through the sleeve and is supported by bearings. Its lower end is fixed to the chopping disk, whereas its upper end is connected to the V-belt pulley through a keyed joint. The blade-shaft sleeve is fixed to the frame. During operation, power is transmitted to the blade shaft through the belt drive, causing the chopping blades and the flexible mowing rope to rotate at high speed. As the machine advances, flexible mowing lines made of galvanized steel wire rope, with a diameter of 4 mm and an effective working length of 400 mm, chop the green manure on the orchard floor. The chopped stems are then discharged to the right side along the direction of travel. The cutting blades primarily sever the thicker stolons and basal portions of the hairy vetch plants.

2.3.1.2 Selection of key design parameters for the green-manure chopping device

Working width of green-manure chopping device. The main functions of the green-manure chopping device are to cut the basal portions of the hairy vetch stems and to chop the tender upper stems and leaves. Its working width should therefore be determined with reference to both the orchard planting pattern and the power of the supporting tractor. Rotary chopping machinery generally requires about 11–15 kW of tractor power per meter of working width. Existing rotary mowers typically have working widths of 1.2–1.65 m for top-drive types and 1.25–3.4 m for bottom-drive types. In this study, the machine was matched with a medium-sized 60 hp tractor. Because the green-manure strip in dwarf apple orchards is about 1.5 m wide and a top-drive configuration was adopted, the overall working width was preliminarily set at 1.6 m to ensure full coverage. As the machine employs two chopping devices, each unit was assigned a working width of 0.8 m.

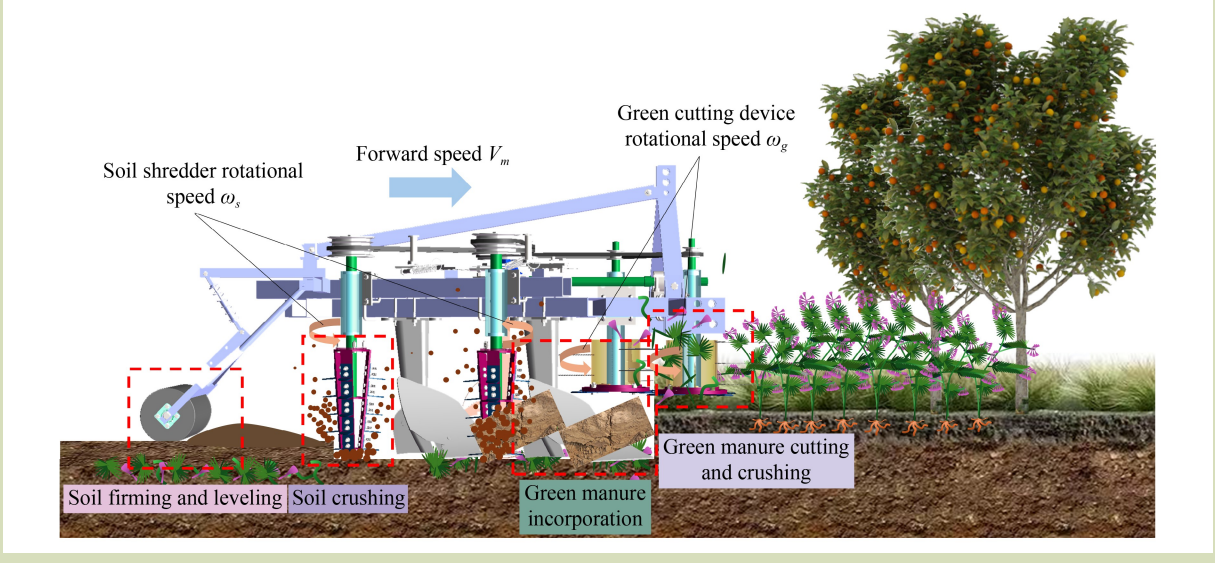


Fig. 3 Schematic diagram of the working process of the orchard green-manure chopping and incorporation machine.

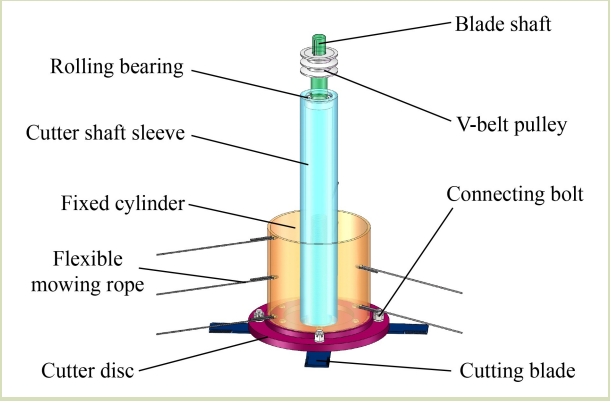


Fig. 4 Schematic diagram of the structure of the green-manure chopping device.

Number of chopping disks, chopping-disk diameters, and number of blades of the green-manure chopping device. The cutter-disk diameter is closely related to the drive configuration. In top-drive mowers, the number of cutter disks should not be excessively large, because too many disks raise the centre of gravity and may reduce stability. Typically, top-drive mowers use one to four disks, and disk diameters usually in the range 500–1500 mm, with 700–900 mm being the most common. Each disk generally carries two to four blades in top-drive configurations and two to three blades in bottom-drive configurations. To avoid unchopped strips, the blade paths of adjacent disks are usually designed to overlap by 30–60 mm[17]. On this basis, and considering the required working width, the present design uses two cutter disks with a diameter of 700 mm, each equipped with four blades.

Rotational speed of the green-manure chopping device. During operation, each blade undergoes a compound motion resulting from disk rotation and forward machine travel. As shown in Fig. 5(a), the ground projection of the blade tip follows a trochoidal trajectory. The continuous chopping paths therefore form a trochoidal working zone with width equal to the outward extension of the blade, as illustrated in Fig. 5(b). To ensure smooth chopping of hairy vetch stems without blockage or entanglement, the absolute velocity at the blade tip must exceed the critical chopping speed[18]. Under unsupported chopping conditions, the minimum critical chopping speed at the blade tip is about 30 m·s^{-1}. Given that the blades in the present design are bolted to the cutter disk, a higher speed is required for stable operation; in practice, the chopping speed should therefore be 50–90 m·s^{-1}. Under orchard field conditions, the forward speed of the machine is usually 4–7 km·h^{-1}. By substituting the maximum forward speed, R = 0.4 m and V_g = 50 m·s^{-1} into $n = \frac{30(V_g + V_m)}{\pi R} > \frac{30(V_{a\min} + V_m)}{\pi R}$, the minimum rotational speed of the chopping device is 1240 r·min^{-1}. Accordingly, the rotational speed of the chopping device was selected in the range of 1200–2000 r·min^{-1} to ensure stable stem chopping without entanglement or blade blockage.

The trajectory equations for the outer tip a and inner tip b of the chopping-blade edge are given by:

$$\begin{cases} x_a = R\cos(\omega_g t + \gamma) \\ y_a = V_m t + R\sin(\omega_g t + \gamma) \end{cases} \tag{1}$$

$$\begin{cases} x_b = r\cos\omega_g t \\ y_b = V_m t + r\sin\omega_g t \end{cases} \tag{2}$$

where x_a and y_a (mm) are the displacements of tip a in the

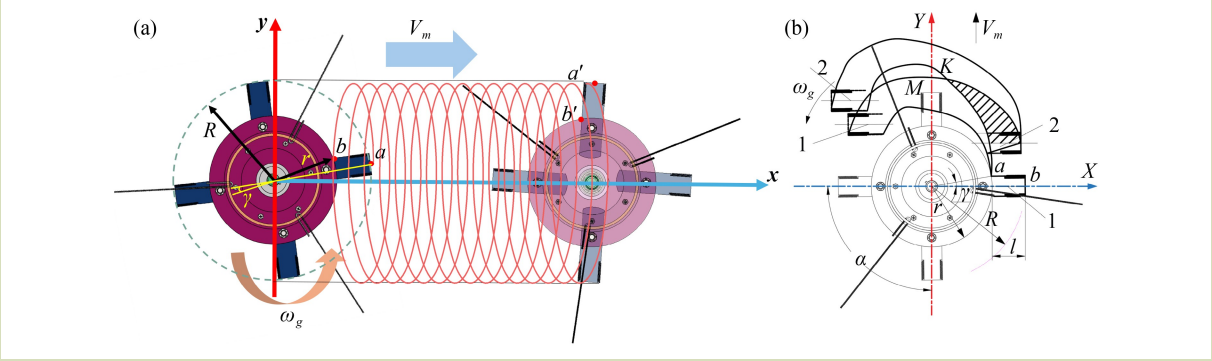


Fig. 5 (a) Trajectory of the chopping blade and (b) Kinematic analysis diagram of the green-manure chopping device.

horizontal and vertical coordinate directions respectively, x_b and y_b (mm) are the displacements of tip b in the horizontal and vertical coordinate directions, respectively, r (mm) is the radius corresponding to the inner tip of the chopping blade, R (mm) is the radius corresponding to the outer tip of the chopping blade, ω_g (rad·s^{-1}) is the angular velocity of the cutter disk, t (s) is the rotation time of the cutter disk, γ (rad) is the angle between the line connecting the inner and outer blade tips and the centre of the cutter disk, and V_{m} (m·s^{-1}) is the forward speed of the machine.

By differentiating Eq. (1) with respect to time t, the velocity equation of the outer tip a of the chopping blade can be obtained as:

$$\begin{cases} V_x{}^a = -R\omega_g \sin(\omega_g t + \gamma) \\ V_y{}^a = V_m + R\omega_g \cos(\omega_g t + \gamma) \end{cases} \tag{3}$$

where $V_x{}^a$ (m·s^{-1}) is the velocity of tip a in the horizontal direction; and $V_y{}^a$ (m·s^{-1}) is the velocity of tip a in the vertical direction.

To ensure smooth chopping and crushing of the hairy vetch stems in the orchard inter-rows, the absolute velocity at the blade tip a must be sufficient to chop the stems without causing blockage or entanglement. The absolute velocity V_a of the outer tip a at any point is given by:

$$\begin{aligned} V_a &= \sqrt{(V_x^a)^2 + (V_y^a)^2} \\ &= \sqrt{(-R\omega_g \sin(\omega_g t + \gamma))^2 + (V_m + R\omega_g \cos(\omega_g t + \gamma))^2} \\ &= \sqrt{R^2\omega_g^2 + 2R\omega_g V_m \cos(\omega_g t + \gamma) + V_m^2} \end{aligned} \tag{4}$$

where V_a (m·s^{-1}) is the absolute velocity of tip a.

The condition for ensuring smooth chopping by the cutting blade is that the minimum value of the absolute velocity (chopping speed) at the outer tip a is greater than the minimum critical chopping speed. The minimum chopping speed occurs when $\omega_g t + \gamma = \pi + 2\pi k$ (k = 0, 1, 2, …, n).

$$V_{a\min} = R\omega_g - V_m \tag{5}$$

where, $V_{a\min}$ (m·s^{-1}) is the minimum chopping speed.

Based on previous studies, the minimum critical chopping speed at the outer blade tip a under unsupported chopping conditions is 30 m·s^{-1}. Given that the blades of the green-manure chopping device are bolted to the cutter disk, a higher chopping speed is required to ensure stable operation. Therefore, the chopping speed V_g should be greater than the minimum critical speed, typically in the range of 50–90 m·s^{-1}. The rotational speed n of the green-manure chopping device is thus given by:

$$n = \frac{30(V_g + V_m)}{\pi R} > \frac{30(V_{a\min} + V_m)}{\pi R} \tag{6}$$

where n (r·min^{-1}) is the rotational speed of the green-manure chopping device, and V_g (m·s^{-1}) is the blade chopping speed.

Under orchard field conditions, the forward travel speed of the machine is typically 4–7 km·h^{-1}. Taking the maximum travel speed and substituting R = 0.4 m and V_g = 50 m·s^{-1} into Eq. (6), the minimum rotational speed of the green-manure chopping device is calculated to be 1240 r·min^{-1}. To ensure that the green-manure chopping device can chop the stems smoothly without entanglement or blade blockage, the rotational speed of the chopping device is selected in the range of 1200–2000 r·min^{-1}.

Blade extension length l. Let α denote the angle interval between two adjacent blades. The area swept by the blades is shown as the shaded region in Fig. 5(b). To avoid missed chopping while minimizing overlap, the condition K_{M} = 0 should be satisfied, that is, $Y_{\mathrm{K}} = Y_{\mathrm{M}}$. Accordingly, when each blade rotates through α, the forward travel distance of the machine should equal the blade extension length l.

$$l = \frac{2\pi r V_m}{m(V_g - V_m)} \approx \frac{2\pi R V_m}{m V_g} \tag{7}$$

In practice, the ratio of forward speed V_m to chopping speed V_g generally ranges from 1/17 to 1/14. As the cutter-disk radius R increases, either the blade extension length l or the number of blades must be increased accordingly. Taking the relevant equations, disk radius, and required working width into account, l was set to 50 mm.

Maximum forward speed of the machine $V_{m\max}$. When the parameters of the green-manure chopping device are determined, the allowable maximum forward travel speed of the machine can be expressed as:

$$V_{m\max} = \frac{lmn}{60} \tag{8}$$

where $V_{m\max}$ (m·s^{-1}) is the maximum forward speed.

2.3.1.3 Establishment and analysis of the ADAMS-based multibody dynamics model

ADAMS multibody dynamics has been widely used in

agricultural engineering to simulate the complex kinematic and dynamic behavior of machine components[19,20]. In this study, ADAMS 2024 was used to analyze the orchard green-manure chopping and incorporation machine at two levels: (1) kinematic analysis of the whole machine, and (2) dynamic analysis of a rigid-flexible coupled model describing the interaction between the chopping device and hairy vetch stems. First, a kinematic model of the whole machine was established in ADAMS, as illustrated in Fig. 6(a). The three-dimensional model created in SolidWorks was exported in .x_t file format and imported into ADAMS. During preprocessing, very small non-functional parts, such as bolts, were removed. Components belonging to the same functional module were then merged into six rigid bodies: the chopping device, soil-pulverizing devices, incorporation plow, frame, firming wheel and depth-limiting wheel. A Q345 steel material model was defined and assigned to the relevant parts. A prismatic joint was used between the frame and the ground to allow rectilinear translation, while revolute joints were defined between the rotating units and the frame. To reproduce power transmission, three belt-drive subsystems were established in ADAMS: one three-pulley drive between the gearbox output shaft and the two green-manure chopping-device shafts, and two additional drives between the gearbox output shaft and the soil-pulverizing shafts. A revolute joint combined with a unidirectional spring element was defined between the firming wheel and the frame to reproduce its actual motion more realistically. Finally, a translational driver was applied to the frame-ground pair and a rotational driver to the gearbox input shaft, thereby completing the virtual prototype.

Determination of belt transmission ratio. Establishing the transmission system shown in Fig. 6(b) required the transmission ratio to be determined. The chopping device and the soil-pulverizing device are driven from the same gearbox output shaft through belt drives and operate simultaneously; the ratio between them was determined from the ratio of the corresponding values of their kinematic speed ranges, i.e., 1200:360 = 2000:600 ≈ 3.33. On this basis, considering the high-speed, low-torque load of the chopping device and the low-speed, high-torque load of the soil-pulverizing device, together with the power of the matched 60 hp tractor, the gearbox first reduces the PTO speed and increases torque, and the belt drives then drive the chopping device and the soil-pulverizing device with ratios of about 4 (step-up) and about 1.2, respectively, realized through the corresponding driving- and driven-pulley diameter ratios. The speeds of the gearbox output shaft, the soil-pulverizing device, and the chopping device are thus in the ratio 1:1.2:4. Because the transmission ratios are fixed, the speeds of the two devices always remain in fixed proportion to the gearbox output shaft speed.

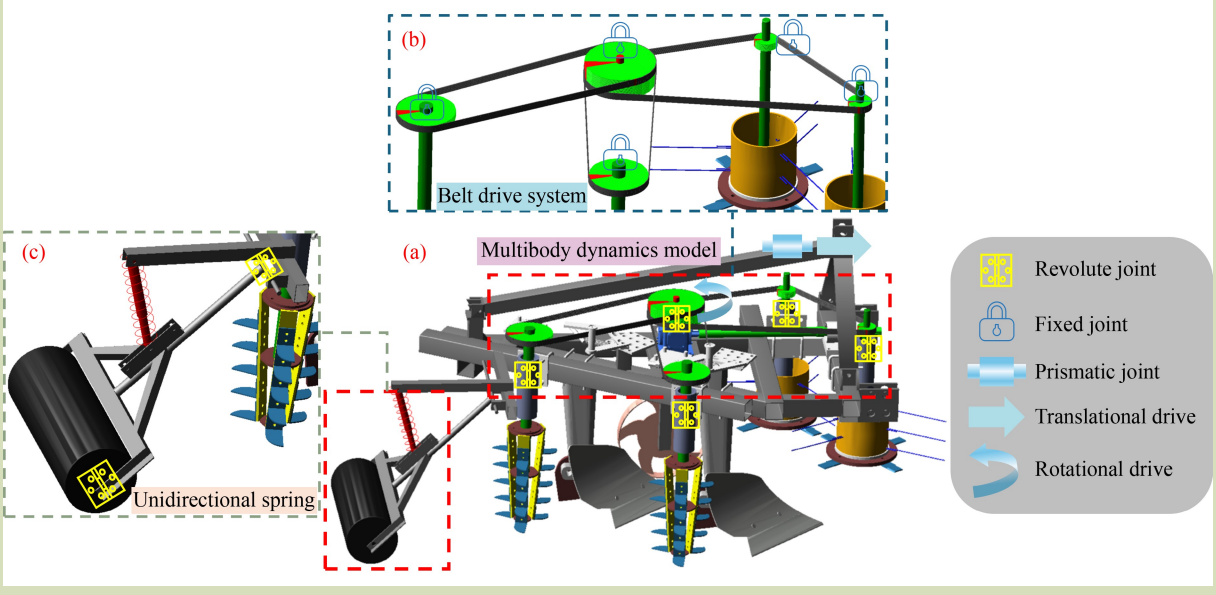


Fig. 6 ADAMS multibody dynamics model of the orchard green-manure chopping and incorporation machine: (a) multibody dynamics model of the whole machine, (b) belt-drive dynamics model, and (c) unidirectional spring model.

Trajectory analysis of the outer blade tip in simulation. As illustrated in Fig. 7(a), when the blade rotational speed is fixed at 2000 r·min^{-1}, the motion trajectory of the blade tip becomes sparser and the swept area decreases as the forward speed increases. As shown in Fig. 7(b), when the forward speed is fixed at 2.0 m·s^{-1}, the motion trajectory of the blade tip becomes denser and the swept area increases with increasing blade rotational speed.

The rigid-flexible coupled interaction model between the chopping device and the hairy vetch stems is shown in Fig. 8.

In ADAMS, flexible-body modeling is commonly implemented in two ways. The first uses flexible beam connections, in which a body is discretized into rigid segments linked by flexible beams. Given that this approach does not represent true continuum flexibility, it is suitable only for geometrically simple components and low-accuracy simulations. The second uses neutral modal files (MNFs), in which the body is meshed and rigid interface regions are created in ADAMS/Flex or in external finite-element software such as HyperMesh/OptiStruct, Abaqus, or ANSYS/APDL. The generated MNF contains modal information that can be imported directly into

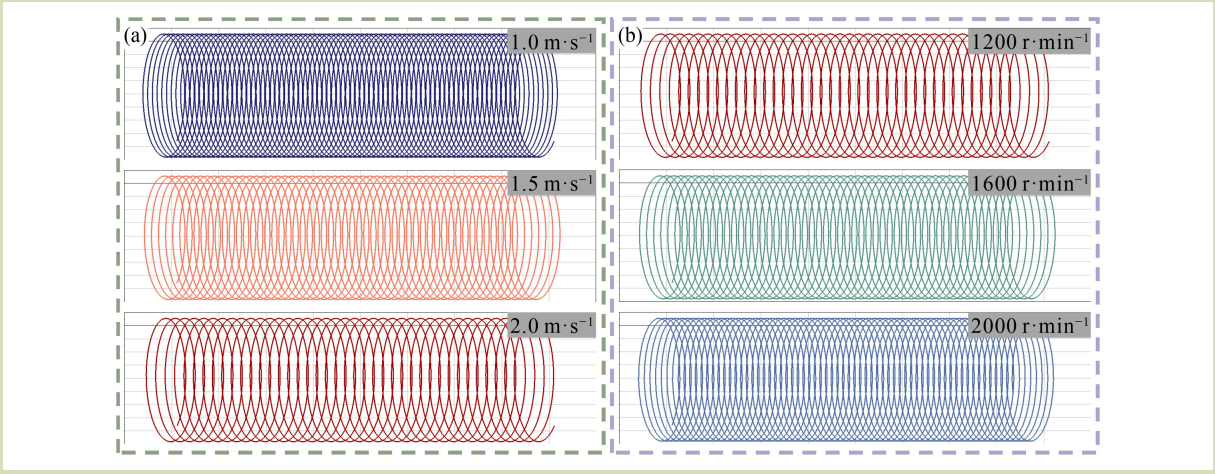


Fig. 7 Distribution of the motion trajectories of the blade outer tip under different machine forward speeds and blade rotational speeds: (a) when the blade rotational speed is constant, the effect of the forward speed on the motion trajectory, and (b) when the forward speed is constant, the effect of the blade rotational speed on the motion trajectory.

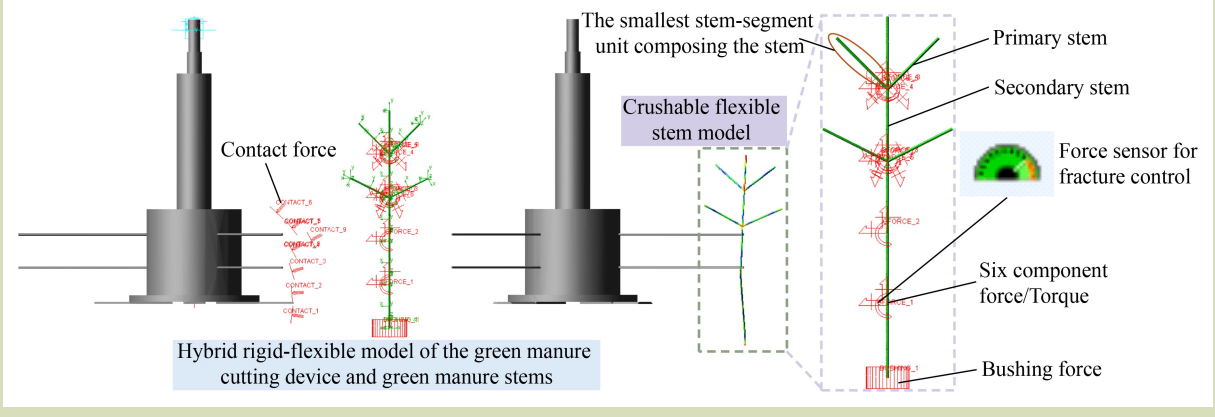


Fig. 8 Rigid-flexible coupled contact model between the green-manure chopping device and hairy vetch stems.

ADAMS for rigid-flexible coupled simulation. Because ADAMS/Flex is limited when handling complex geometries, external finite-element software is generally preferred for higher-accuracy flexible-body modeling.

Processing hairy vetch presents distinctive biomechanical challenges that cannot be represented realistically by a rigid-rigid contact model[21]. During chopping, the stems undergo elastic and plastic deformation before fracture occurs. A rigid-flexible model is therefore required, and accurate stem modeling becomes critical. Because the chopping device acts mainly on stems rather than on leaves or flowers, the plant model was simplified to include only the primary and secondary stems. A geometric model of the stems was first created in SolidWorks and exported in .step file format. The same model was then imported into HyperMesh for finite-element preprocessing, where a mesh size of 1 mm was adopted and RBE2 rigid regions were created at both ends of each stem segment. OptiStruct was used to compute the first 20 Craig-Bampton modes and generate a flexible stem model with 20 modal shapes. The resulting flexible bodies were then imported into ADAMS to replace the corresponding rigid bodies in the rigid-flexible coupled simulation. However, because ADAMS flexible bodies cannot directly simulate material failure, stem fracture still had to be modeled separately.

To overcome the limitation that flexible bodies in ADAMS cannot directly simulate material failure or stem fracture, this study proposes a novel fracture-controlled rigid-flexible coupling method. This method combines flexible-body modeling with six-component force/torque connections, six-component force/torque sensors, and logic-based control functions. The four-step modeling procedure was as follows. (1) Mechanical tests, including tensile, shear, bending and torsional stiffness tests, were first performed to obtain the displacement-force curves, angle-torque curves, and fracture thresholds of hairy vetch stems. The tests were conducted on stems sampled at the full-flowering stage, with diameters of 4–6 mm, and 10 replicates were performed for each loading direction. The slope of the displacement-force curve was used to determine the stiffness K, while the slope of the angle-torque curve was used to determine the torsional stiffness KT. The results are shown in Table 1. For computational feasibility, the mean mechanical parameters and fracture thresholds within this diameter range were used in the simulation. This simplification represents the average fracture response of the stems, but does not capture individual variations caused by stem diameter, moisture content, maturity or local structural defects. Therefore, the simulation results were interpreted mainly as the overall interaction mechanism and relative variation trends under different operating parameters. The model is applicable to full-flowering hairy vetch stems with diameters of about 4–6 mm under the orchard operating conditions considered in this study. For other species, growth stages, moisture conditions or diameter ranges, the mechanical parameters and fracture thresholds should be re-measured and recalibrated. (2) The flexible stem model was not constructed as a single continuous plant but was assembled from flexible stem segments of 50–100 mm long. Adjacent stem segments were connected using six-component force/torque connections, which represent the internal forces and moments transmitted between segments. A six-component force/torque sensor was placed at each connection to monitor force and moment components in all degrees of freedom. When any monitored force or torque reached a predefined fracture threshold, the sensor was triggered. An IF-based logic function was then used to deactivate the internal six-component force/torque connection at that segment, thereby simulating stem fracture. By combining flexible deformation with force-controlled failure, this approach reproduced the interaction between the green-manure chopping device and the stems more realistically. (3) Contact between the green-manure chopping device and the flexible stems was modeled using the impact function method, which is more suitable than the penalty method for intermittent contacts. Normal contact

Table 1 Mechanical property parameters of the hairy vetch stem

Dimension	Parameter type			
	K (N·mm^{-1})	Fracture force (N)	KT (N·mm/°)	Fracture torque (N·mm)
X	4.68 ± 0.73	17.8	0.12	13.4
Y	4.27 ± 0.87	17.2	0.12	13.4
Z	6.76 ± 1.12	23.0	0.56	62.1

parameters included contact stiffness, damping, force exponent and penetration depth, while tangential parameters included the static and dynamic friction coefficients. (4) Driving conditions and boundary constraints were then defined. The root of each stem was connected to the ground through a bushing force element. The green-manure chopping device was assigned appropriate constraints and driving functions to achieve translational motion relative to the ground and rotational motion about its axis. The transient simulation was conducted for 0.12 s with 1200 simulation steps. For computational feasibility, the mean values for stems within this diameter range were used as the fracture thresholds in the simulation. ADAMS/Solver was configured with the GSTIFF integrator and the SI2 formulation; the damping coefficient of the connector elements was taken empirically as one-tenth of the stiffness ($C = K/10$).

The force-control logic used for fracture identification is expressed as:

$$\begin{aligned}&-(K\times \mathrm{DX}(Stem1.center, Stem2.center, Stem2.center)\\&-C\times \mathrm{VX}(Stem1.center, Stem2.center, Stem2.center))\\&\times(\mathrm{IF}(\mathrm{SENVAL}(SENSOR_1)-F_x: 1,1,0))\end{aligned} \quad (9)$$

where K (in N·mm^{-1}) is the stiffness coefficient, *Stem1_centre* is the top-centre point of stem segment 1, *Stem2_centre* is the bottom-centre point of stem segment 2, C (in N·s·mm^{-1}) is the damping coefficient, set $K/10$, *SENSOR_1* is the sensor used to detect the connection force between stem segment 1 and stem segment 2, and F_x (in N) is the fracture force.

The state function of the sensor is GFORCE(*GFORCE_1*, 0, 1, 0). *GFORCE_1* is the six-component forces/torques connecting stem segments 1 and 2.

Figure 9 shows the deformation and fracture process of the hairy vetch stems. Before contact, the plant remained in its initial state. When the flexible mowing rope first contacted the stem at 0.05 s, high local stress developed at the contact site. At 0.06 s, the stem underwent substantial deformation, and by 0.07 s the primary stem had bent severely while the upper secondary stems had begun to fracture. Between 0.08 and 0.11 s, the primary stem also fractured. The six force and moment components (F_x, F_y, F_z, T_x, T_y and T_z) transmitted between stem segments 1 and 2 were extracted and plotted, as shown in Fig. 10. The results indicate that fracture was initiated when the X-direction force component first reached the fracture threshold, indicating that stem failure was dominated by shear. The single-factor simulation results are summarized in Fig. 11. The number of fractured stem segments decreased as forward speed increased from 1.1 to 1.9 m·s^{-1}, because the number of impacts and chopping events per unit time decreased. In contrast, the number of fractured segments increased markedly when rotational speed increased from 1200 to 2000 r·min^{-1}, owing to both higher contact forces and more impacts per unit time. Ground clearance produced no obvious change in the number of fractured stem segments.

Single-factor simulation test. To further investigate the effects of the forward speed, rotational speed, and ground clearance of the green-manure chopping device on the chopping

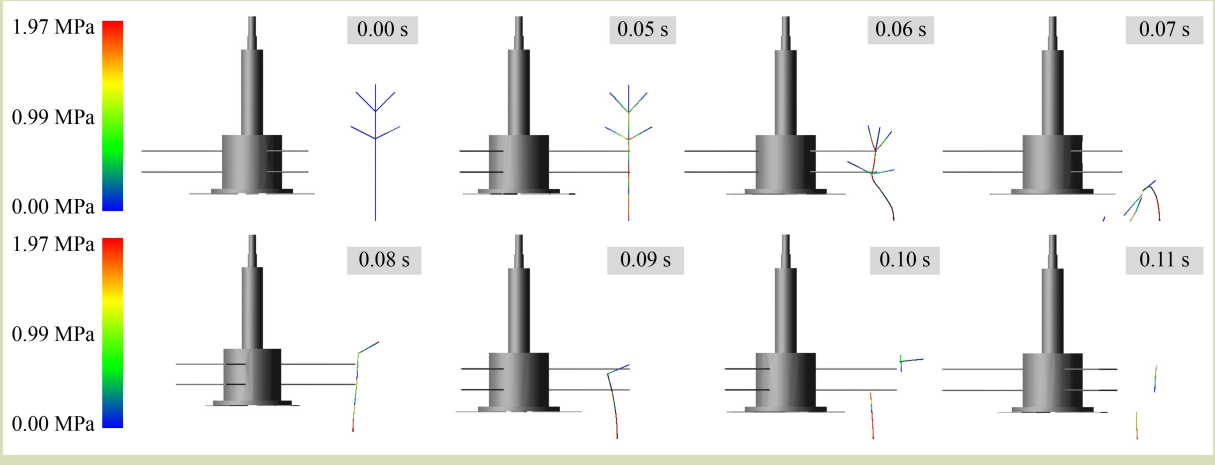


Fig. 9 Simulated chopping process of hairy vetch stems by the green-manure chopping device.

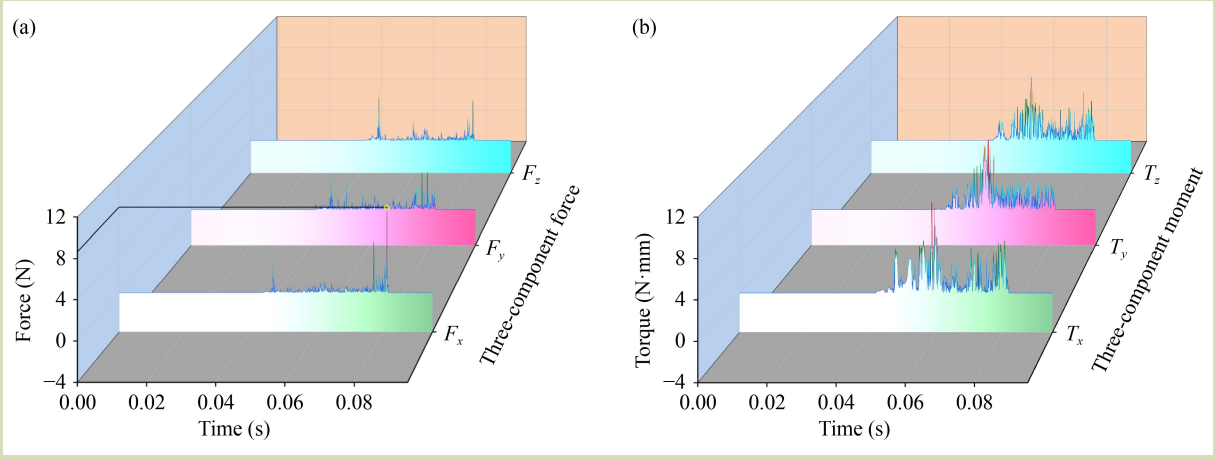


Fig. 10 (a) Time-history curves of the six force components between stem segments 1 and 2, and (b) time-history curves of the six torque components between stem segments 1 and 2.

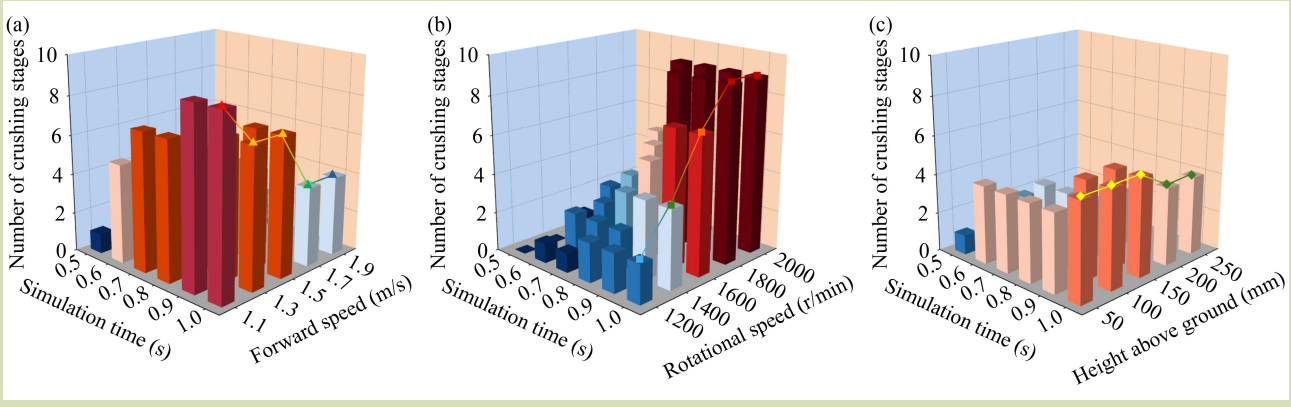


Fig. 11 Results of the single-factor simulation tests: (a) plot of the number of fractured stem segments versus the forward speed, (b) plot of the number of fractured stem segments versus the rotational speed, and (c) plot of the number of fractured stem segments versus the height above ground.

performance, a single-factor simulation test was conducted using the number of fractured stem segments as the evaluation index. The forward speed was set to 1.1–1.9 m·s^{-1}, the rotational speed to 1200–2000 r·min^{-1} and the height above ground to 50–250 mm. The range of ground clearance was determined according to the growth characteristics of hairy vetch and the field operating conditions. The lower bound of 50 mm was chosen to accommodate the uneven ground surfaces of orchards and to avoid the blades gouging the ground, while still chopping as close to the ground as possible. Hairy vetch is a trailing, creeping legume, with a natural height of about 300–600 mm at full flowering, and its thick creeping stems and basal portions are mostly distributed within about 250 mm above the ground. When the ground clearance exceeds 250 mm, the proportion of stems that can be chopped drops markedly and stubble increases, which no longer meets the requirement of close-to-ground cutting and adequate incorporation. The ground clearance was therefore set to 50–250 mm. The levels of the experimental factors are shown in Table 2.

Results of the single-factor simulation tests. The experimental

Table 2 Factors and levels for the single-factor simulation test

No.	Factor		
	Forward speed (m·s^{-1})	Rotational speed (r·min^{-1})	Height above ground (mm)
1	1.1	1200	50
2	1.3	1400	100
3	1.5	1600	150
4	1.7	1800	200
5	1.9	2000	250

results were plotted as bar charts, as shown in Fig. 11. As shown in Fig. 11(a), the number of fractured stem segments decreased as the forward speed increased from 1.1 to 1.9 m·s^{-1}. This is because the number of chopping events per unit time is reduced, resulting in insufficient stem chopping. As shown in Fig. 11(b), when the rotational speed increases from 1200 to 2000 r·min^{-1}, the number of fractured stem segments increases significantly. The main reason is that higher rotational speed leads to larger contact forces between the chopping device and the stems, producing stronger damage. Meanwhile, the increased number of impacts per unit time allows the stems to be more fully crushed. From Fig. 11(c), the number of fractured stem segments shows no obvious change with increasing height above ground.

2.3.2 Design of the incorporation plow

2.3.2.1 Working principle of the incorporation plow

As illustrated in Fig. 12, the incorporation plow mainly consists of a plowshare, moldboard, beam and landside. Its function is to break the plow pan and bury the chopped stems, leaves and other residues left on the orchard inter-row surface by the chopping device. This promotes deeper incorporation and accelerates decomposition. A soil-pulverizing device is mounted on the right-hand side of the plow body to break the clods lifted by the plow and to cover the furrow evenly.

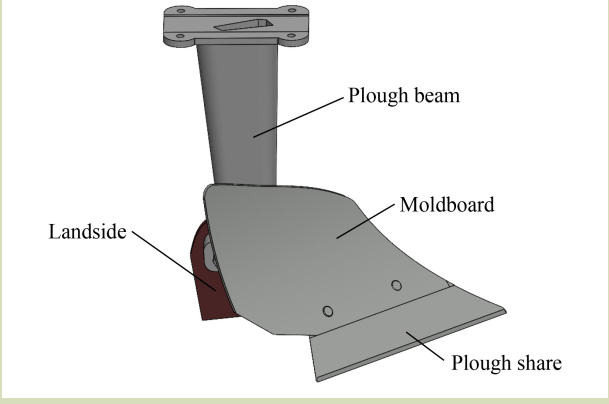


Fig. 12 Structural diagram of the incorporation plow.

2.3.2.2 Design parameters of the incorporation plow

Number of incorporation plows and working width. According to orchard agronomic requirements, incorporating leguminous green manure at a depth of 150–200 mm is most favorable for decomposition and nutrient release. With reference to the width-depth ratio of the furrow and to GB/T 14225-2008 (moldboard plow), the working width of a single plow body was determined on the basis of the maximum incorporation depth of 200 mm. The working width of one plow body was therefore set to 300 mm. Considering the traction capacity of the supporting tractor, two plow bodies were selected, giving a total working width of 600 mm.

Plow-body surface contour. As illustrated in Fig. 13, the wing-edge line EF was determined from the 225 mm × 300 mm furrow cross-section produced by the plow. The landside edge line BC was obtained from the working width, and the maximum calculated height of the top-edge line CE was 346 mm. AB denotes the projection of the plowshare edge, whereas the wing line AF is determined from the plan-view contour of the plow body surface. The projected contour of the plow body in the forward direction is therefore CE.

Analysis of the variation pattern of the generator-line angle. Given that the soil between orchard rows is relatively compact and cohesive, a semi-helical (inversion-type) plow body was

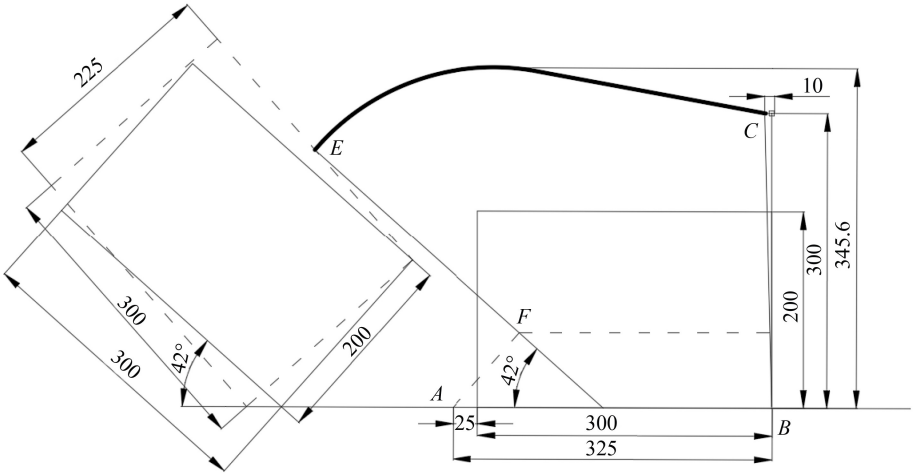


Fig. 13 Design diagram of the plow-body surface contour.

adopted to ensure complete inversion of the soil clods. The wing section of the plow body was truncated to facilitate incorporation. The initial and boundary conditions of the generator-line angle were $\theta_0 = 38^\circ$, $\theta_{min} = 35^\circ$, and $\theta_{max} = 49^\circ$ at $Z_{max} = 305$ mm, with $Z_1 = 55$ mm. The variation from θ_0 to θ_{min} followed a linear law, divided into five equal segments, with a decrease in generator-line angle of $\Delta\theta = 36'$ per segment. For the section from θ_{min} to θ_{max}, the spacing of the horizontal generator lines was 50 mm, and the distance between the generator lines corresponding to θ_{min} and θ_{max} is:

$$\begin{cases} \Delta y = y_{max} - y_{min} = \dfrac{x^2}{2P} = \dfrac{(Z_{max} - Z_1)^2}{2P} \\ m = \dfrac{\Delta\theta}{\Delta y} = (\theta_{max} - \theta_{min}) \cdot \dfrac{2P}{(Z_{max} - Z_1)^2} \\ y_x = \dfrac{x^2}{2P} \\ \theta_x = \theta_{min} + m y_x \end{cases} \quad (10)$$

The resulting variation in generator-line angle is shown in Fig. 14(a).

Variation of the guide curve. Given that a semi-helical plow body was used, the guide-curve height h was related to the height of the top edge of the plow body and was set to 340 mm. To enhance soil inversion, the installation angle ε of the plowshare was set to 20°, and the length of the initial straight section S was 50 mm. Thus, the tangent angle β is:

$$\beta = 90^\circ + \varepsilon - \Delta\varepsilon = 90^\circ + 20^\circ - 5^\circ = 105^\circ \quad (11)$$

After these parameters had been determined, the guide curve of the plow body was drawn using the envelope method, as shown in Fig. 14(b).

$$x^2 + 0.012102xz + 1.326211z^2 + 405.287489x - 1113.518225z = 0 \quad (12)$$

2.3.3 Design of the soil-pulverizing device

2.3.3.1 Structure and working principle of the soil-pulverizing device

As illustrated in Fig. 15, the soil-pulverizing device mainly consists of a V-belt pulley, a soil-pulverizing blade shaft, fixing plates, a soil-pulverizing blade, cutter disks and a soil-pulverizing blade shaft sleeve. The soil-pulverizing blades are bolted to the fixing plates, which are welded to the circumference of the cutter disks. The cutter disks are rigidly and coaxially connected to the soil-pulverizing blade shaft, which is supported by bearings inside the soil-pulverizing blade shaft sleeve. The soil-pulverizing blade shaft sleeve is fixed to the frame, and the V-belt pulley is connected to the shaft via a key. During operation, power is transmitted to the soil-pulverizing device through the V-belt drive. As the machine advances, the rotating blades pulverize the clods overturned by the incorporation plow, thereby achieving fine soil pulverization.

2.3.3.2 Selection of key design parameters for the soil-pulverizing device

Rotational radius and rotational direction of the soil-pulverizing

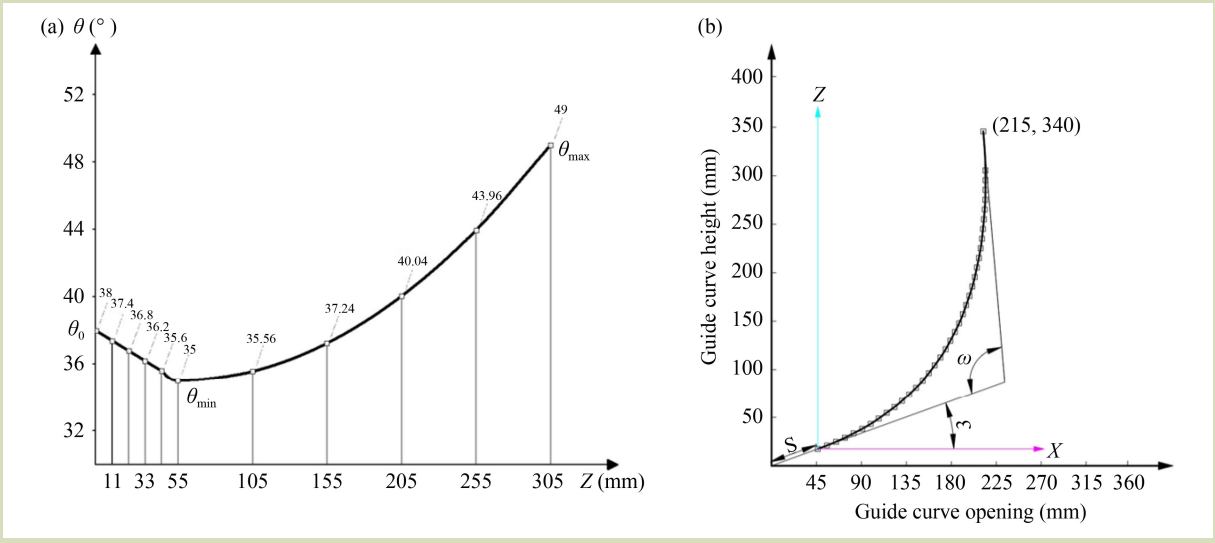


Fig. 14 (a) Variation pattern of the generator-line angle and (b) guide curve and fitted curve of the plow body.

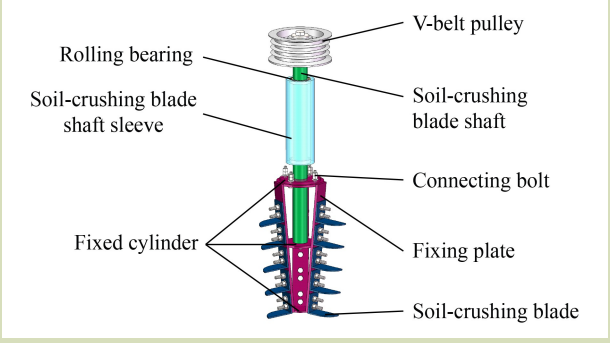


Fig. 15 Structure diagram of the soil-pulverizing device.

blade roller. A smaller blade-roller radius helps to balance the device and reduce power consumption, and is generally selected within the range of 150–180 mm. A variable-radius configuration, with a larger radius in the upper part and a smaller radius in the lower part, can reduce power demand further. The design therefore adopted a variable-radius blade roller with an upper radius of 140 mm and a lower radius of 80 mm. When viewed from above, the soil-pulverizing device rotates clockwise.

Rotational speed of the soil-pulverizing blade roller. Higher blade-roller speed generally improves soil-pulverizing performance, but it also increases power consumption. As illustrated in Fig. 16, the blades move forward with the machine while simultaneously rotating around the blade roller, and their actual motion is the superposition of these two movements. The displacement equations of the blade tip c in the horizontal and vertical directions are:

$$\begin{cases} x_c = R_s \cos \omega_s t \\ y_c = V_m t + R_s \sin \omega_s t \end{cases} \tag{13}$$

where x_c and y_c are the displacements of tip c in the horizontal and vertical coordinate directions respectively (mm); R_s is the rotational radius of the blade tip c (mm); t is the motion time (s); ω_s is the rotational speed of the soil-pulverizing blade roller (rad·s^{-1}).

By differentiating Eq. (13) with respect to time t, the velocity equations of the blade tip c in the horizontal and vertical directions are obtained as:

$$\begin{cases} V_x^c = -R_s \omega_s \sin \omega_s t \\ V_y^c = V_m + R_s \omega_s \cos \omega_s t \end{cases} \tag{14}$$

where V_x^c is the velocity of tip c in the horizontal direction (m·s^{-1}); V_y^c is the velocity of tip c in the vertical direction (m·s^{-1}). V_m is the forward speed (m·s^{-1}).

The absolute velocity of blade tip c is given by:

$$V_c = \sqrt{(V_x^c)^2 + (V_y^c)^2} = \sqrt{R_s^2 \omega_s^2 + 2R_s \omega_s V_m \cos \omega_s t + V_m^2} \tag{15}$$

where V_c is the absolute velocity of blade tip c (m·s^{-1}).

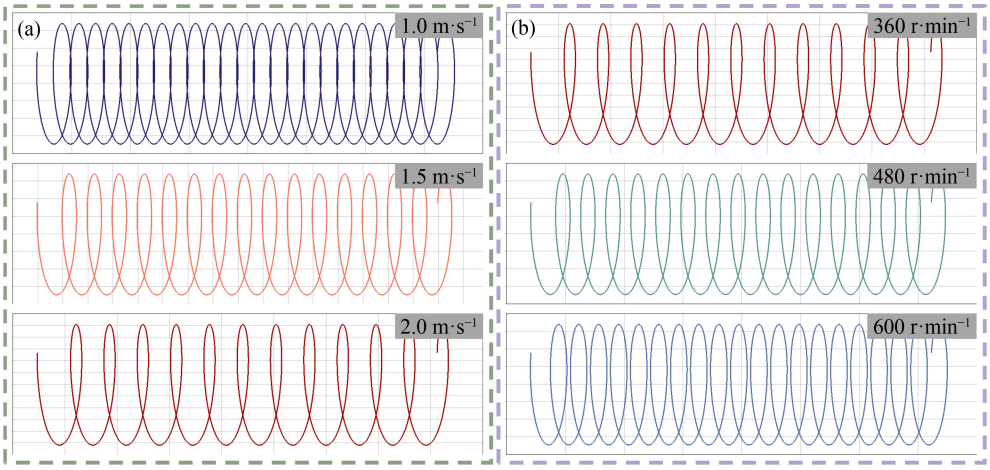


Fig. 16 Distribution of the motion trajectories of the soil-pulverizing blade tip *c* under different machine forward speeds and soil-pulverizing blade rotational speeds, (a) when the soil-pulverizing blade rotational speed is constant, the effect of the forward speed on the motion trajectory, (b) when the forward speed is constant, the effect of the soil-pulverizing blade rotational speed on the motion trajectory.

To ensure that the blade can effectively pulverize soil clods, the motion trajectory of blade tip *c* should form a curtate cycloid. Therefore, the soil-pulverizing speed ratio λ must satisfy $\lambda > 1$, and λ is calculated as:

$$\lambda = \frac{\omega_s R_s}{V_m} > 1 \tag{16}$$

where λ is the soil-pulverizing speed ratio.

Orchard machinery usually travels at 4–7 km·h^{-1}. On this basis, the rotational speed of the soil-pulverizing device was selected as 360–600 r·min^{-1}, and the suitability of this range was further verified by ADAMS simulation, as illustrated in Fig. 16. As illustrated in Fig. 16(a), when the rotational speed of the soil-pulverizing blade was 360 r·min^{-1}, as the forward speed increases, the swept area by the soil-pulverizing blade decreases. When the forward speed reached its maximum of 2.0 m·s^{-1}, the trajectory curve remained a curtate cycloid. Similarly, when the forward speed is 2.0 m·s^{-1}, as the rotational speed of the soil-pulverizing blade increases, the trajectory curve of the soil-pulverizing blade becomes denser. Even when the rotational speed of the soil-pulverizing blade reaches the minimum value of 360 r·min^{-1}, the trajectory curve of the soil-pulverizing blade remained a curtate cycloid.

Number of soil-pulverizing blades. A greater number of blades on each disk generally improves soil-pulverizing performance, but it also increases power consumption and may aggravate grass entanglement and blockage. To balance pulverization quality and operational stability, three blades were installed on each cutter disk.

2.4 Strength verification of the orchard green-manure chopping and incorporation machine

The machine is rear-mounted on the tractor through a three-point hitch and is powered by the tractor PTO during field operation. Because orchards are often located in hilly and mountainous regions, the machine must withstand uneven terrain and severe loading conditions. Static strength verification of the three-dimensional virtual prototype was therefore conducted before prototype manufacture to identify potential weak points and to confirm whether the structure could withstand severe orchard operating conditions. The machine was made of Q345 steel, and static analysis under extreme working conditions was performed in HyperMesh and OptiStruct to evaluate structural safety.

2.4.1 Method for establishing the finite-element model of the orchard green-manure chopping and incorporation machine

The three-dimensional model of the machine was imported into HyperMesh in .step file format and meshed using 5 mm

tetrahedral elements. Bolted connections were replaced by RBE2 rigid elements, and welded regions of the frame were modeled using tied surface contacts, as illustrated in Fig. 17. RBE2 elements and SPC constraints were also defined at the three-point hitch locations. A Q345 steel material model was then created and assigned to the corresponding components. To improve solution accuracy, a second-order mesh was used.

During field operation, the machine is subjected not only to its own weight but also to additional inertial loads generated by rapid acceleration, deceleration and turning of the tractor[22]. These effects were represented as equivalent accelerations in the X (lateral), Y (longitudinal) and Z (vertical) directions, with gravitational acceleration taken as 9.81 $m \cdot s^{-2}$. The material properties of the main structural components are given in Table 3.

2.4.2 Extreme operating conditions

Typical operating conditions for the tractor-mounted machine include straight travel, turning, and bumping. Based on the relevant literature, the most common and the most severe loading cases were selected for linear static structural analysis. The four analyzed conditions are given in Table 4.

2.4.3 Simulation results and analysis

The strength analysis results under the four operating conditions are illustrated in Fig. 18. Under Condition 1, the maximum stress was 251 MPa and occurred at the upper hitch point of the three-point linkage, giving a safety factor of 1.37. Under Condition 2, the maximum stress was 181 MPa, also located on the inner side of the upper hitch point, and the corresponding safety factor was 1.91. Under Condition 3, the maximum stress was 110 MPa at the connection between the firming device and the frame, with a safety factor of 3.14. Under Condition 4, the maximum stress was 99.9 MPa, again located at the connection between the firming device and the frame, with a safety factor of 3.45. These results indicate that the machine satisfied the strength requirements under the analyzed extreme operating conditions.

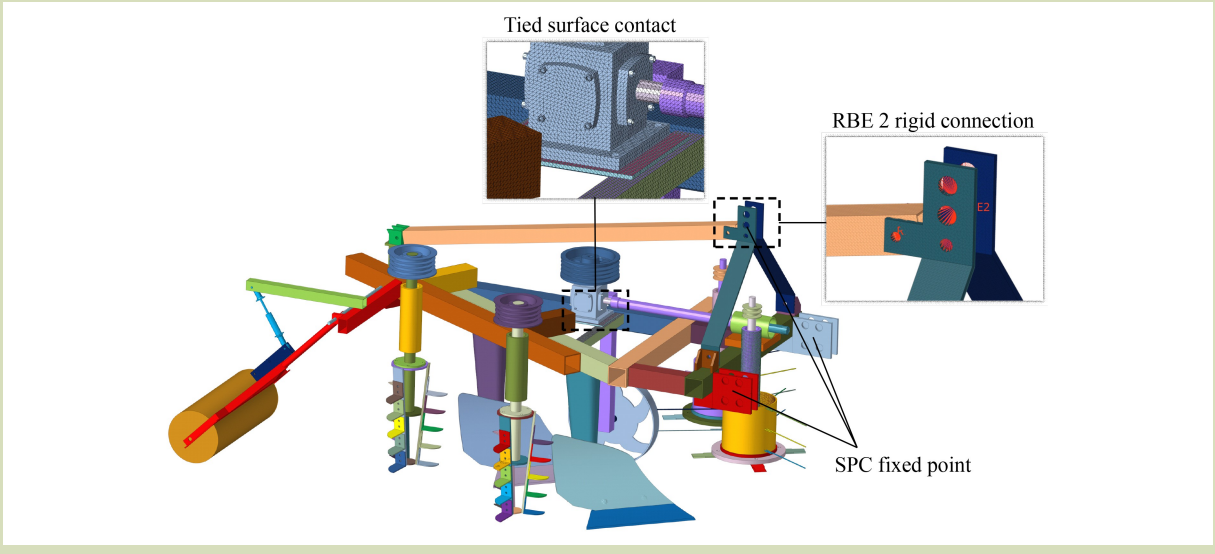


Fig. 17 Establishment of the finite-element model of the orchard green-manure chopping and incorporation machine.

Table 3 Q345 steel material property parameters

Material	Young's modulus (MPa)	Yield strength (MPa)	Poisson's ratio
Q345	206,000	345	0.289

Table 4 Operating condition parameters

No.	*X* (g)	*Y* (g)	*Z* (g)	Condition
1	0.0	0.0	2.5	Field moderate bumping
2	0.3	0.2	1.5	Lateral swing/turning + high vertical load (left)
3	0.0	−0.5	1.8	Lateral swing/turning + high vertical load (right)
4	0.0	0.5	1.8	Extreme vertical condition

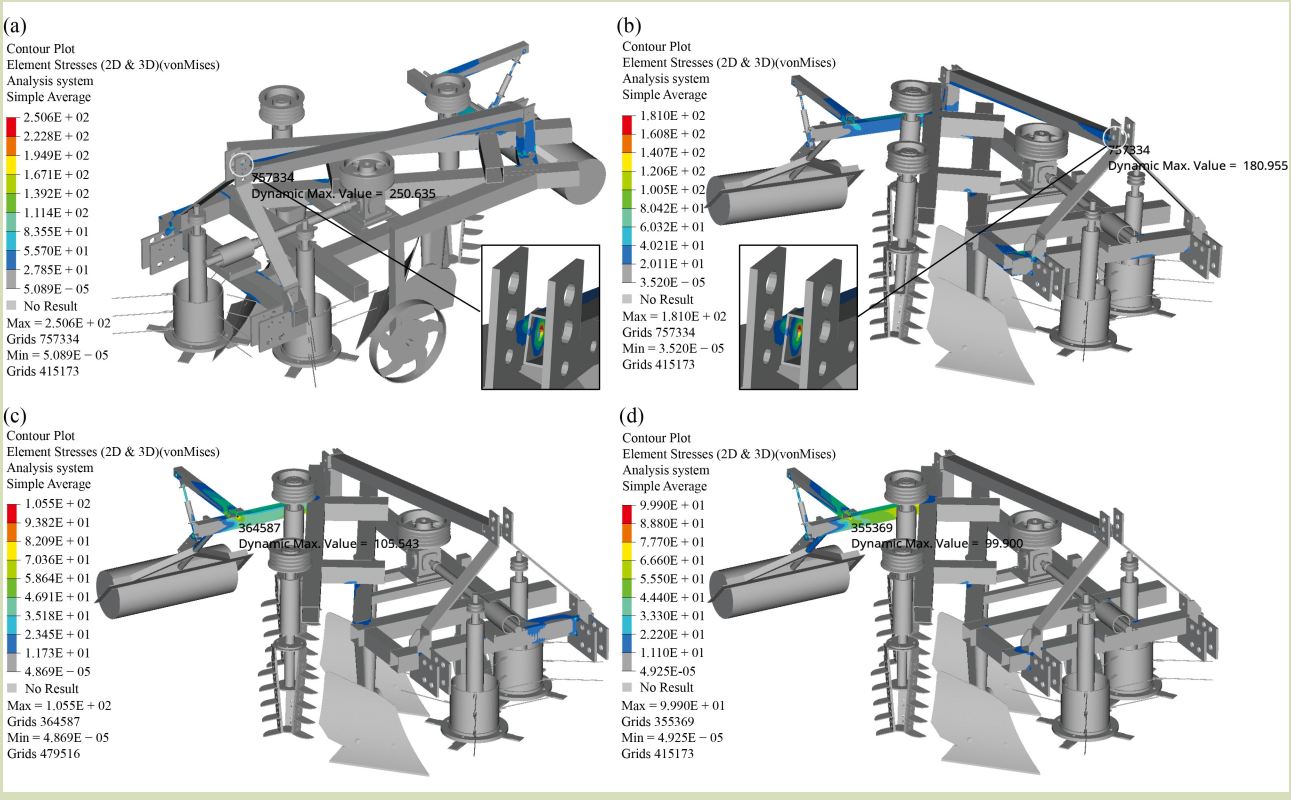


Fig. 18 Stress distribution diagrams of the orchard green-manure chopping and incorporation device under severe operating conditions: (a–d) conditions 1–4.

2.5 Field optimization tests

2.5.1 Test materials

Field experiments were conducted using the hairy vetch cultivar Mengtiao No. 1. The test site was located in the orchard of Wuba Agricultural Technology Co., Ltd., on Nongyuan 10th Road in Yangling Demonstration Zone, Shaanxi Province. The trials were conducted on 20 April 2025. The orchard covered 33.3 ha (500 mu), with a row spacing of 3.5 m, plant spacing of 1.5 m, and a green-manure strip width of 1.5 m. The soil was sandy loam, as shown in Fig. 19(a).

2.5.2 Test equipment and method

The experimental equipment comprised the self-developed orchard green-manure chopping and incorporation prototype shown in Fig. 19(b), a Dongfanghong MF554 tractor (60 hp), a tachometer, an Ohaus moisture analyzer, and a Yingheng H1-



Fig. 19 Test materials and test process, (a) field test case, (b) orchard green-manure chopping and incorporation prototype, and (c) field test process.

50 kg electronic balance. The stem chopping, incorporation, soil pulverization and leveling processes observed during the field tests are shown in Fig. 19(c).

No specific standard for evaluating the operational quality of orchard green-manure incorporation machinery has yet been issued in China. The prototype was therefore assessed with reference to the test methods and performance indices specified in GB/T 10938-2008 (rotary mowers) and GB/T 6678-2001 (straw crushing and returning machines). On this basis, the qualified stem-length rate and stem incorporation rate were selected as the key performance indicators. The qualified stem-length rate was defined as the mass percentage of stems with chopping lengths that met the specified requirement within a sampling area. Five sampling points were evenly distributed along each travel path, and each sampling area was 1 m^2. All crushed hairy vetch plants within each sampling area were collected and weighed to obtain M_{ti}. The unqualified stems were then separated and weighed to obtain M_{ni}. The mean value from the five sampling points was taken as the result for each trial. The stem incorporation rate was defined as the ratio of the mass of hairy vetch stems buried below the soil surface to the total stem mass within the sampling area. Stem fragments exposed on the soil surface were collected and weighed as M_{si}, and the total mass of all pulverized hairy vetch plants within the sampling area was recorded as M_{ti}.

The qualified stem-length rate was calculated qualified stem-length rate for each sampling point, and the average value of the five sampling points is taken as the final result for each trial. The calculation formula for the qualified stem-length rate is:

$$\begin{cases} Q_i = \dfrac{M_{ti} - M_{ni}}{M_{ti}} \times 100\% \\ Q = \dfrac{\sum_i^5 Q_i}{5} \end{cases} \tag{17}$$

where Q_i (%) is the qualified stem-length rate at the *i-th* sampling point, M_{ti} (kg) is the total mass of hairy vetch stems at the *i-th* sampling point, M_{ni} (kg) is the total mass of unqualified hairy vetch stems at the *i-th* sampling point and Q (%) is the qualified stem-length rate for a single trial.

The stem incorporation rate was defined as the ratio of the mass of hairy vetch stems incorporated below the soil surface to the total stem mass within the measurement area. The test procedure was as follows: five sampling points were selected along each travel direction, with each sampling point covering an area of 1 m^2. The mass of stem fragments exposed on the soil surface was collected, weighed, and recorded as M_{si}. The total mass of all pulverized hairy vetch plants within the sampling area was weighed and recorded as M_{ti}. The stem incorporation rate was then calculated as:

$$\begin{cases} T_i = \dfrac{M_{ti} - M_{si}}{M_{ti}} \times 100\% \\ T = \dfrac{\sum_i^5 T_i}{5} \end{cases} \tag{18}$$

where T_i (%) is the stem incorporation rate at the *i-th* sampling point, M_{si} (kg) is the mass of hairy vetch stems exposed on the soil surface at the *i-th* sampling point and T (%) is the stem incorporation rate for a single trial.

2.5.3 Box-Behnken test

Given that the machine uses a belt-drive system, the rotational speeds of the chopping device and soil-pulverizing device are proportional to the rotational speed of the gearbox output shaft. The gearbox output shaft speed was therefore used as an independent factor in place of the individual unit speeds. Based on the single-factor simulation results, machine forward speed and green-manure chopping-device rotational speed had significant effects on stem chopping, whereas ground clearance had little effect. Accordingly, machine forward speed, X_1, gearbox output shaft speed, X_2, and plow incorporation depth, X_3 were selected as the experimental factors. The response variables were the qualified stem-length rate, Y_1 and the stem incorporation rate, Y_2. A three-factor, three-level Box-Behnken design was used to analyze the effects of the factors and their interactions, and to identify the optimum parameter combination. The test factors and levels of the Box-Behnken test are shown in Table 5.

3 Results and analysis

3.1 Box-Behnken test results and analysis

According to the factor coding given in Table 5, a Box-Behnken design was generated in Design-Expert 13. A total of 17 field tests were then conducted, and the experimental matrix and results are given in Table 6.

Regression analysis in Design-Expert 13 yielded quadratic regression equations describing the relationships among forward speed X_1, shaft rotational speed X_2, plow incorporation depth X_3, the qualified stem-length rate Y_1 and the stem incorporation rate Y_2. The equations were:

$$Y_1 = 85.91 - 6.54X_1 + 7.57X_2 + 0.03X_3 + 2.87X_1X_2 + 0.03X_1X_3 - 0.03X_2X_3 + 0.52X_1^2 - 2.15X_2^2 - 1.19X_3^2 \quad (19)$$

$$Y_2 = 90.94 - 0.70X_1 + 2.36X_2 + 5.63X_3 - 0.75X_1X_2 + 0.16X_1X_3 - 1.39X_2X_3 + 0.10{X_1}^2 - 5.95{X_2}^2 - 0.43{X_3}^2 \quad (20)$$

The ANOVA (analysis of variance) results for Eq. (19) are given in Table 7. For model Y_1, the regression term was highly significant ($p < 0.01$) whereas the lack-of-fit term was not significant ($p = 0.2801$), indicating that the model was adequate. Factors X_1 and X_2 had highly significant effects on Y_1 whereas X_3 was not significant. Among the interaction terms, only X_1X_2 was highly significant. Among the quadratic terms, only X_2^2 had a highly significant effect. The influence of the factors on Y_1 decreased in the order of gearbox output shaft speed X_2, forward speed X_1 and incorporation depth X_3.

The ANOVA results for Eq. (20) are shown in Table 8. Model Y_2 was highly significant ($p < 0.01$), and the lack-of-fit term was not significant ($p = 0.700$), indicating an adequate model fit. The factors X_2 and X_3 had highly significant effects on Y_2, and X_1 had a significant effect on Y_2. Among the interaction terms, X_2X_3 had a highly significant effect on Y_2, X_1X_2 had a significant effect and X_1X_3 was not significant. Among the quadratic terms, only X_2^2 had a highly significant effect on Y_2; the other quadratic terms were not significant. The influence of the test factors on model Y_2 decreased in the order: incorporation depth X_3, gearbox output shaft speed X_2 to forward speed X_1.

3.2 Interaction analysis

The response surfaces derived from the regression equations are shown in Fig. 20. Figure 20(a) shows the effect of the interaction between X_1 and X_2 on the response Y_1. It can be seen that when the gearbox output shaft speed X_2 was kept constant, the qualified stem-length rate Y_1 gradually decreased with increasing forward speed X_1. When the rotational speed X_2 was at a low level, the effect of forward speed X_1 on Y_1 was significant. When X_2 was at a high level, the influence of X_1 on

Table 5 Test factors and levels of the Box-Behnken test

Code	Factor		
	Forward speed X_1 (m·s^{-1})	Rotational speed X_2 (r·min^{-1})	Incorporation depth X_3 (mm)
−1	1.0	300	100
0	1.5	400	150
1	2.0	500	200

Table 6 Results of the Box-Behnken test

No.	Factor			Qualified stem-length rate Y_1 (%)	Stem incorporation rate Y_2 (%)
	X_1	X_2	X_3		
1	0	0	0	87.1	91.2
2	1	0	−1	79.4	84.2
3	1	−1	0	66.5	83.0
4	0	0	0	85.6	91.1
5	0	0	0	86.3	91.8
6	−1	0	1	91.0	96.8
7	1	1	0	87.4	86.1
8	0	0	0	86.1	90.6
9	1	0	1	79.6	95.3
10	−1	1	0	96.3	88.7
11	−1	0	−1	90.9	86.2
12	0	0	0	84.5	90.1
13	0	−1	1	75.0	89.4
14	0	1	−1	90.2	82.5
15	0	1	1	90.1	91.4
16	−1	−1	0	87.0	82.5
17	0	−1	−1	75.0	74.9

Table 7 ANOVA for regression model Y_1

Source	Qualified stem-length rate Y_1				
	Sum of square	df	Mean square	F-value	p-value
Model	860.25	9	95.58	72.17	$< 0.0001^{**}$
X_1	341.78	1	341.78	258.04	$< 0.0001^{**}$
X_2	458.44	1	458.44	346.12	$< 0.0001^{**}$
X_3	0.0078	1	0.0078	0.0059	0.9409
X_1X_2	32.95	1	32.95	24.88	0.0016^{**}
X_1X_3	0.0042	1	0.0042	0.0032	0.9565
X_2X_3	0.0036	1	0.0036	0.0027	0.9599
X_1^2	1.15	1	1.15	0.8654	0.3832
X_2^2	19.36	1	19.36	14.64	0.0065^{**}
X_3^2	6.00	1	6.00	4.53	0.0709
Residual	9.27	7	1.32		
Lack of fit	5.38	3	1.79	1.84	0.2801
Pure error	3.89	4	0.9737		
Total	869.97	16			

Note: ** Indicates $p < 0.01$, denoting an extremely significant difference; and * indicates $p < 0.05$, denoting a significant difference.

Table 8 ANOVA for regression model Y_2

Source	Stem incorporation rate Y_2				
	Sum of square	df	Mean square	*F*-value	*p*-value
Model	464.15	9	51.57	159.12	< 0.0001**
X_1	3.92	1	3.92	12.09	0.0103*
X_2	44.65	1	44.65	137.77	< 0.0001**
X_3	253.80	1	253.80	783.08	< 0.0001**
X_1X_2	2.27	1	2.27	6.99	0.0332*
X_1X_3	0.0870	1	0.0870	0.2685	0.6203
X_2X_3	7.76	1	7.76	23.93	0.0018**
X_1^2	0.0382	1	0.0382	0.1179	0.7414
X_2^2	149.05	1	149.05	459.88	< 0.0001**
X_3^2	0.7776	1	0.7776	2.40	0.1653
Residual	2.27	7	0.3241		
Lack of Fit	0.6227	3	0.2076	0.5043	0.6997
Pure Error	1.65	4	0.4115		
Total	466.41	16			

Note: ** Indicates $p < 0.01$, denoting an extremely significant difference; and * indicates $p < 0.05$, denoting a significant difference.

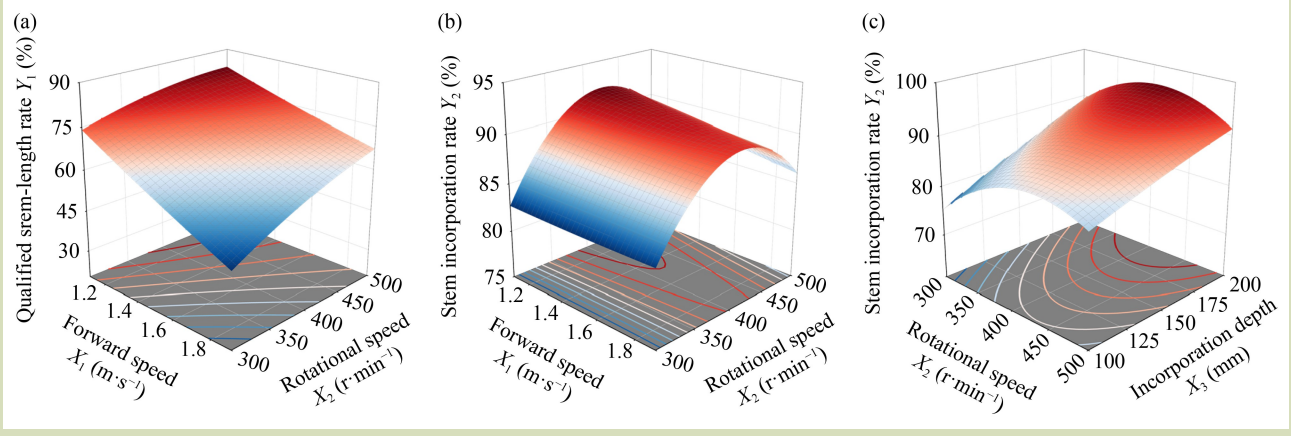


Fig. 20 Effects of factor interactions: (a) $X_1 \times X_2$ on Y_1; (b) $X_1 \times X_2$ on Y_2; and (c) $X_2 \times X_3$ on Y_2.

Y_1 was reduced. At a constant forward speed X_1, Y_1 increased with increasing rotational speed X_2. When X_1 was at a low level, X_2 had a significant effect on Y_1; when X_1 was at a high level, the influence of X_2 on Y_1 weakened. Overall, the interaction between X_1 and X_2 had a strong effect on Y_1. Figure 20(b) shows the effect of the interaction between X_1 and X_2 on the response Y_2. When the rotational speed X_2 was fixed, the effect of forward speed X_1 on the stem incorporation rate Y_2 was minimal; Y_2 remained almost unchanged with increasing X_1, regardless of whether X_2 was at a low, medium, or high level. At a constant forward speed X_1, the effect of rotational speed X_2 on Y_2 was significant. As X_2 increased, Y_2 first increased and then decreased, reaching its maximum at a rotational speed of 400 r·min^{-1}. The X_1–X_2 interaction had a relatively weak effect

on Y_2. As shown in Fig. 20(c), when the incorporation depth X_3 was held constant, Y_2 first increased and then decreased with increasing rotational speed X_2. When X_2 was constant, Y_2 increased gradually with increasing incorporation depth X_3. When X_2 was at a low level, the effect of X_3 on Y_2 was stronger; when X_2 was at a high level, the influence of X_3 on Y_2 weakened.

3.3 Optimization of experimental parameters

The optimization function in Design-Expert 13 was used to solve Eqs. (19) and (20). Maximizing both Y_1 and Y_2 yielded the optimum factor combination of forward speed X_1, gearbox output shaft speed X_2, and incorporation depth X_3. The optimization objective and constraints are given in Eq. (21). The predicted optimum conditions were a forward speed of 1.1 m·s^{-1}, a gearbox output shaft rotational speed of 457 r·min^{-1}, and an incorporation depth of 190 mm, under which Y_1 and Y_2 were predicted to be 94.2% and 95.1%, respectively.

$$\begin{cases} \max Y_1(X_1, X_2, X_3) \\ \max Y_2(X_1, X_2, X_3) \\ \begin{cases} 1.0 < X_1 < 2.0 \\ 300 < X_2 < 500 \\ 100 < X_3 < 200 \end{cases} \end{cases} \tag{21}$$

3.4 Verification test

To verify the optimized parameter combination, six validation tests were conducted. Given that the experimental machine could not be adjusted exactly to the theoretical optimum parameter values, the actual parameter values were set as close as possible to the optimum solution based on practical conditions: a forward speed of 1.1 m·s^{-1}, a gearbox output shaft speed of 450 r·min^{-1} and an incorporation depth of 190 mm. Under these conditions, the qualified stem-length rate was 91% ± 1.5% and the stem incorporation rate was 91% ± 2.1%, with relative errors of 3.4% and 4.3% with respect to the predicted values of 94.2% and 95.1%, respectively.

Based on the residual mean square and prediction variance of the regression models, the 95% prediction intervals at the theoretical optimum were further calculated. The 95% prediction interval for Y_1 was [90.7%, 97.7%], and the measured mean of 90.7% falls within this interval, indicating that the model prediction for Y_1 is statistically consistent with the field results. The 95% prediction interval for Y_2 was [93.3%, 96.8%], and the measured mean of 91.3% falls below the lower bound. Two reasons are identified for this. First, the inevitable deviation between the actual operating parameters and the theoretical optimum introduces additional prediction error. Second, in field verification, the stem incorporation rate is affected by spatial variability in soil texture, nonuniform plant distribution, and fluctuations in burial depth; the measured variability (SD = 2.05%) substantially exceeds the model residual (RMSE = 0.57%), and the 95% prediction interval of the model does not fully capture this additional field variability. Despite this, the relative prediction error for Y_2 of 3.99% remains within an acceptable range for field experiments with agricultural machinery, and the optimized parameter combination demonstrates practical reliability. However, the tendency of the model to slightly overestimate the stem incorporation rate is acknowledged as one of the limitations of this study.

3.5 Discussion

Compared with existing orchard green-manure equipment, the present machine has clear advantages in functional integration and operational performance. Most existing machines of this type can perform only part of the workflow, such as stem chopping or soil turning, and generally suffer from insufficient stem incorporation, multi-pass operation, and a lack of accompanying soil pulverization and firming units, which makes their operation relatively complicated. By chopping and pulverizing, incorporating and covering, soil pulverizing, and leveling and firming together in a single pass, the present machine achieves a qualified stem-length rate of 91% ± 1.5% and a stem incorporation rate of 91% ± 2.1%, which addresses the insufficient incorporation and multi-pass operation of the equipment mentioned above. To further clarify the advantages of the proposed machine, a quantitative comparison with representative orchard green-manure or orchard grass-management implements is presented in Table 9. Because the evaluation indices reported in different studies are not completely identical, the closest comparable indicators are given, including chopping or cutting quality, incorporation or coverage performance, incorporation depth, and operation integration.

In terms of method, to deal with the difficulty that flexible bodies in ADAMS cannot directly simulate material failure, the

Table 9 Quantitative comparison between the proposed machine and representative similar implements

Implement	Main operation function	Main performance indicator	Incorporation performance	Operation characteristics
Orchard inter-row green-manure mower reported by Zhao et al.[13]	Chopping, throwing, and firming	Qualified crushing-length rate 93.6% when the qualified length was less than 100; 97.2% when the qualified length was less than 150 mm	Not reported	Mainly performs chopping and surface treatment, without deep soil inversion or incorporation
Offset straw-returning machine for orchard green manures reported by Zhang et al.[23]	Crushing, furrowing, burying, and soil covering	Crushing length qualification rate of 91.2%	Average coverage rate of 90.9% at a furrowing depth of 190 mm	Achieves good covering performance, but the operation mainly focuses on furrowing and soil covering
Proposed machine in this study	Stem chopping and incorporation, soil pulverization and firming	Qualified stem-length rate of 91% ± 1.5%	Stem incorporation rate of 91% ± 2.1% at an incorporation depth of 190 mm	Integrates chopping, deep incorporation, soil pulverization, and firming in a single pass

proposed fracture-controlled rigid-flexible coupling method breaks the internal force connections between stem segments in real time through sensor triggering and IF logic functions, reproducing the process from elastic-plastic deformation to fracture. On this basis, it is clear that the X-direction force component reaches the fracture threshold first and that stem failure is dominated by shear, which also provides a useful reference for the chopping simulation of similar biomass stems.

The trends in the simulation and field results are generally consistent, indicating that the simulation offers useful reference value for actual operation. The single-factor simulation identified forward speed and rotational speed as the dominant factors affecting stem breakage, with ground clearance being negligible; this guided the field Box-Behnken design, in which ground clearance was excluded, forward speed and gearbox output shaft speed were retained, and incorporation depth was introduced for the incorporation stage. The simulated trends, viz, an increase in fractured stem segments with rotational speed and a decrease with forward speed, are consistent with the field response, where the qualified stem-length rate rose with rotational speed and fell with forward speed, indicating that the proposed fracture-controlled rigid-flexible coupling model reflects the general trends of the stem-chopping process. As the simulation addressed only chopping and pulverizing, the incorporation, soil-pulverizing, and firming stages were evaluated experimentally; the two approaches are complementary and jointly underpin the final parameter selection.

It should be noted that the field validation in this study was conducted in a dwarf apple orchard with sandy loam soil, using hairy vetch at the full-flowering stage as the target green-manure crop. Therefore, the optimized operating parameters and performance results reported here are mainly applicable to similar orchard conditions, soil texture and crop characteristics. When the machine is used in heavier clay soils, looser sandy soils, different soil moisture conditions or with other green-manure species, its chopping, incorporation, soil-pulverizing and firming performance may change. Future work should therefore extend field tests to different orchard soil types, soil moisture levels, green-manure species and growth stages. In addition, the effects of variable stem density, biomass and soil resistance on machine performance should be further examined. On this basis, the structural parameters and operating settings of the machine can be refined to improve its adaptability and reliability under a wider range of orchard green-manure incorporation conditions.

4 Conclusions

This study addressed the problems of inadequate stem chopping, insufficient incorporation depth, and limited functional integration in existing orchard green-manure machinery by developing a dedicated machine capable of stem chopping, incorporation, soil pulverization, and firming in a single pass. An ADAMS model of the whole machine and an ADAMS/OptiStruct rigid-flexible contact model of the chopping process were established. Structural strength under severe working conditions was evaluated by finite-element analysis, and the operating parameters were optimized and validated through field experiments. Four main conclusions arise from this study.

Firstly, the key components, namely the green-manure chopping device, incorporation plow, and soil-pulverizing device, were designed, and their main parameters were determined. The kinematics of the chopping device and soil-pulverizing device were analyzed theoretically, yielding the allowable machine forward and rotational speed ranges of the two working units.

Secondly, an ADAMS multibody dynamics model of the whole machine was established, and the effects of forward speed and rotational speed on the blade-tip trajectories of the chopping and soil-pulverizing devices were analyzed. By coupling ADAMS and OptiStruct, a rigid-flexible contact model was developed for the interaction between the chopping device and hairy vetch stems. Within the simulation framework, stem fracture was represented through the combined use of sensors, control functions and six-component force/moment connections. The single-factor simulations showed that forward speed and rotational speed strongly affected the degree of stem breakage, whereas ground clearance had only a minor effect. As forward speed increased, the number of fractured stem segments decreased; as rotational speed increased, the number of fractured stem segments increased.

Thirdly, a finite-element model of the machine was established in HyperMesh and OptiStruct, and structural performance under severe operating conditions was assessed. Across four representative extreme working conditions, the highest simulated stress was 251 MPa, the minimum safety factor was 1.38, and the critical location was the upper hitch point of the three-point linkage. Under these analyzed conditions, the machine satisfied the strength requirements.

Finally, field experiments used the qualified stem-length rate and the stem incorporation rate as response variables, and machine forward speed, gearbox output shaft speed and incorporation depth as experimental factors in a Box-Behnken design. For chopping quality, the factor effects decreased in the order of gearbox output shaft speed, forward speed, and incorporation depth. For stem incorporation rate, the order was incorporation depth, gearbox output shaft speed and forward speed. The optimum practical settings were a forward speed of 1.1 $m \cdot s^{-1}$, a gearbox output shaft speed of 450 $r \cdot min^{-1}$, and an incorporation depth of 190 mm. Under these conditions, the qualified stem-length rate was 91% ± 1.5%, and the stem incorporation rate was 91% ± 2.1%, indicating satisfactory performance under the tested conditions.

It is recommended that future research focus on two aspects. First, experiments under different soil textures and green-manure species should be conducted to further examine the operational adaptability of the machine. Second, evaluations of power consumption, blade wear and long-term reliability should be added to assess the overall performance more comprehensively, thereby supporting the further improvement, application and promotion of orchard green-manure chopping and incorporation equipment.

Acknowledgements

This study was supported by Shaanxi Green Manure Production and Utilization Fund, China (20230092503554) and Shaanxi Key Research and Development Program, China (2023-YBNY-210).

Compliance with ethics guidelines

Chun Wang, Yujing Zhou, Yizhe Yang, Yongchao Shao, and Weiguo Zhang declare that they have no conflicts of interest or financial conflicts to disclose. This article does not contain any studies with human or animal subjects performed by any of the authors.

REFERENCES

1. Ma D K, Yin L N, Ju W L, Li X K, Liu X X, Deng X P, Wang S W. Meta-analysis of green manure effects on soil properties and crop yield in northern China. *Field Crops Research*, 2021, **266**: 108146

2. Song J R, Jiao Y, Wu W Q, Wang X F, Gu K M, Liu Q, Bao S S, Kong X Q, Yue S C, Li S Q, Shen Y F. Legume straw incorporation with optimal nitrogen fertilizer improves soil quality and reduces the carbon footprint of farmland

ecosystems in semiarid areas. *Industrial Crops and Products*, 2025, **230**: 121081

3. da Cunha Honorato A, Maciel J F A, de Assis R M A, Nohara G A, de Carvalho A A, Pinto J E B P, Bertolucci S K V. Combining green manure and cattle manure to improve biomass, essential oil, and thymol production in *Thymus vulgaris* L. *Industrial Crops and Products*, 2022, **187**: 115469
4. Lyu H, Li Y, Wang Y L, Wang P F, Shang Y P, Yang X H, Wang F, Yu A Z. Drive soil nitrogen transformation and improve crop nitrogen absorption and utilization—A review of green manure applications. *Frontiers in Plant Science*, 2024, **14**: 1305600
5. Ma L, Wang D T, Zhang L, Ge Y, Liu Y Q, Cheng Y X, Jiang X F. Green manure application improves insect resistance of subsequent crops through the optimization of soil nutrients and rhizosphere microbiota. *iScience*, 2024, **27**(7): 110320
6. Qiu H L, Yin W, Li P, Zhang D K, Wei J G, Zhao L H, Wan P X, Fan Z L, Hu F L, Nan Y Y, Chai Q, Chen H Y, Abdalla M, Smith P. Green manure returning improves wheat yield and N utilization efficiency by minimizing N loss in Oasis irrigation area of China. *The Crop Journal*, 2025, **13**(6): 1884–1897
7. Wang P F, Yu A Z, Wang F, Wang Y L, Lyu H, Shang Y P, Yang X H, Liu Y L, Yin B, Zhang D L, Chai Q. Nitrogen reduction by 20% with green manure retention reduces soil evaporation, promotes maize transpiration and improves water productivity in arid areas. *Field Crops Research*, 2024, **315**: 109488
8. Li S B, Huan X L, Wang T Y, Hui Y T, You Y, Wang D C. Biomechanical properties and discrete element modeling of PSR stalks during silage harvest. *Computers and Electronics in Agriculture*, 2024, **217**: 108644
9. Shi Y Y, Sun X, Wang X C, Hu Z C, Newman D, Ding W M. Numerical simulation and field tests of minimum-tillage planter with straw smashing and strip laying based on EDEM software. *Computers and Electronics in Agriculture*, 2019, **166**: 105021
10. Zheng Y J, Jiang S J, Chen B T, Lyu H T, Wan C, Kang F. Review on technology and equipment of mechanization in hilly orchard. *Transactions of the Chinese Society for Agricultural Machinery*, 2020, **51**(11): 1–20 (in Chinese)
11. Zhang Q Z, Yang B H, Liu X Y, Liao J A, Zhao J F, Su G D, Wang L, Xu M D. Design and experiment of an all-in-one machine for crushing and rolling between rows in orchard. *Journal of Agricultural Mechanization Research*, 2025, **47**(10): 123–129 (in Chinese)
12. Wang X Y, Liao J A, Wang Y Z, Zhao J F, Li K, Ye R, Yang Y X, Lan H P, Ma X T. Design and test of 2BH-6 green fertilizer rotary tillage mixed planter. *Journal of Agricultural Mechanization Research*, 2021, **43**(9): 66–71 (in Chinese)
13. Zhao J F, Xi L Q, Liao J A, Li K, Ma X T, Tan Z M. Design and experiment of green manure mower between orchard rows. *Journal of Chinese Agricultural Mechanization*, 2021, **42**(7): 42–49 (in Chinese)
14. Gao X D, He N N, Jia R H, Hu P, Zhao X N. Redesign of dryland apple orchards by intercropping the bioenergy crop canola (*Brassica napus* L.): achieving sustainable intensification. *GCB Bioenergy*, 2022, **14**(3): 378–392
15. Kong W Y, Geng B H, Yan W H, Xia J, Xu W K, Zhao N, Guo Z F. Full-length transcriptomes reconstruction reveals intraspecific diversity in hairy vetch (*Vicia villosa* Roth) and smooth vetch (*V. villosa* Roth var. *glabrescens*). *Plants*, 2024, **13**(23): 3291
16. Müller J, Levien R, Trein C R, Sequinatto L, Mazurana M, Stürmer S L K, Pietrzacka R. Physical and chemical attributes of a typic ultisol in organic citrus orchard with weed control between the lines. *Revista Brasileira de Fruticultura*, 2011, **33**(4): 1127–1134 (in Portuguese)
17. Guo Z, Wang D C, Wu B, Wang G H, Wang Z Q, Liu L D. The design and simulation of the test bench of a disc mower. *China Dairy Cattle*, 2016, (2): 31–34 (in Chinese)
18. O'Dogherty M J, Gale G E. Laboratory studies of the effect of blade parameters and stem configuration on the dynamics of cutting grass. *Journal of Agricultural Engineering Research*, 1991, **49**: 99–111
19. Liu L, Wang X L, Zhang X C, Zhong X K, Wei Z C, Geng Y L, Cheng X P, Zhao K L, Bai M Y. Determination and verification of parameters for the discrete element modelling of single disc covering of flexible straw with soil. *Biosystems Engineering*, 2023, **233**: 151–167
20. Chen T, Yi S J, Li Y F, Tao G X, Qu S M, Li R. Establishment of discrete element model and parameter calibration of alfalfa stem in budding stage. *Transactions of the Chinese Society for Agricultural Machinery*, 2023, **54**(5): 91–100 (in Chinese)
21. Liao Y T, Liao Q X, Zhou Y, Wang Z T, Jiang Y J, Liang F. Parameters calibration of discrete element model of fodder rape crop harvest in bolting stage. *Transactions of the Chinese Society for Agricultural Machinery*, 2020, **51**(6): 73–82 (in Chinese)
22. Li M T, Li J L, He L, He J, Hu L, Lyu C. Analysis of the track system in bumpy unstructured hard road environment by vibration test. *International Journal of Agricultural and Biological Engineering*, 2022, **15**(4): 163–171
23. Zhang Q Z, Zhao J F, Yang X W, Wang L, Su G D, Liu X Y, Shan C, Rahim O, Yang B H, Liao J A. Design and testing of an offset straw-returning machine for green manures in orchards. *Agriculture*, 2024, **14**(11): 1932